Applied Catalysis B: Environmental 129 (2013) 13–29

Contents lists available at SciVerse ScienceDirect

Applied Catalysis B: Environmental

journal homepage: www.elsevier.com/locate/apcatb

Transformation products and reaction kinetics in simulated solar light photocatalytic degradation of propranolol using Ce-doped TiO_2

Javier Santiago-Morales[a], Ana Agüera[b], María del Mar Gómez[b], Amadeo R. Fernández-Alba[b,c], Jaime Giménez[d], Santiago Esplugas[d], Roberto Rosal[a,c,*]

[a] Department of Chemical Engineering, University of Alcalá, E-28771 Alcalá de Henares, Spain
[b] Department of Analytical Chemistry, University of Almería, E-04010 Almería, Spain
[c] Advanced Study Institute of Madrid, IMDEA-Agua, Parque Científico Tecnológico, E-28805, Alcalá de Henares, Madrid, Spain
[d] Department of Chemical Engineering, University of Barcelona, E-08028, Barcelona, Spain

ARTICLE INFO

Article history:
Received 26 June 2012
Received in revised form 5 September 2012
Accepted 13 September 2012
Available online 20 September 2012

Keywords:
Propranolol
Solar photocatalysis
Transformation products
Liquid chromatography
Mass spectrometry

ABSTRACT

The visible light photocatalytic degradation of propranolol was studied using cerium doped titanium dioxide, a catalyst that showed an increased light absorption in the visible region. The experiments were carried out in ultrapure water and in a biologically treated wastewater from the secondary effluent of a treatment plant spiked with propranolol. The best results were obtained for a cerium loading of 0.5 wt.% and a bulk catalyst concentration of 0.14 g/L, with which propranolol became essentially depleted after 1.5 h of irradiation. The extent of mineralization reached 17.4% after 6 h on stream under the same conditions. Both oxidation on catalyst holes and reaction with hydroxyl radicals contribute to propranolol depletion, but for the reaction conditions tested in this study, the first mechanism predominated and accounted for 60% of the propranolol rate constant. The runs performed in wastewater matrix led to a very low photocatalytic rate compared with pure water, which was attributed to the presence of radical scavengers and competing substances. Over thirty reaction intermediates were detected by means of exact mass measurements performed by liquid chromatography coupled to quadrupole-time-of-flight mass spectrometry (LC-ESI-QTOF–MS/MS) based on the characteristic fragmentation of oxidation by-products. Their relative abundance was also assessed in catalytic and non-catalytic runs. The most abundant transformation products could be attributed to the cleavage of the ether bond of propranolol. Other compounds detected derived from the addition of hydroxyl groups to the aromatic nuclei or to the ring-opening attack of hydroxyl radicals on the naphthol moiety. Finally, the toxicity of oxidized mixtures was determined using the green algae *Pseudokirchneriella subcapitata* and the bioluminescent marine bacterium *Vibrio fischeri*. Although the toxicity of treated mixtures tended to decrease as propranolol was depleted, mixtures treated in pure water may lead to the accumulation of toxic transformation products.

1. Introduction

The incomplete removal of pharmaceuticals and other emerging pollutants in conventional wastewater treatment plants (WWTP) has been identified as the main route by which anthropogenic pollutants reach aqueous environments [1]. As a consequence, the presence of pharmaceuticals has become ubiquitous in natural waters, even to the extent of entering drinking water facilities [2]. Some of the adverse effects of these pollutants on ecosystems have been reported but the risk associated with chronic exposure remains essentially unknown [3]. The presence of anthropogenic pollutants in treated wastewaters also endangers reuse, which is becoming a major issue in view of the growing water scarcity [4]. The occurrence of β-blockers has been repeatedly reported in recent years in the effluents of many WWTP around the world [5–7]. It has been clearly established that conventional wastewater treatments using activated sludge are not effective in completely removing propranolol. Maurer et al. reported removal efficiencies in the 28–35% range for propranolol in two WWTP located in the vicinity of Zürich [8]. Rosal et al. monitored the primary and final effluents of a WWTP located in Alcalá de Henares, Madrid, performing monthly analyses on time-composite samples over a one-year sampling period [9]. They obtained average concentrations of atenolol, metoprolol and propranolol of 1025 ng/L, 19 ng/L, and 36 ng/L, respectively, with very low removal efficiencies which did not exceed 15% for atenolol and were even lower for the other two.

* Corresponding author at: Department of Chemical Engineering, University of Alcalá, E-28771 Alcalá de Henares, Spain. Tel.: +34 918856395; fax: +34 918855088.
E-mail address: roberto.rosal@uah.es (R. Rosal).

0926-3373/$ – see front matter © 2012 Elsevier B.V. All rights reserved.
http://dx.doi.org/10.1016/j.apcatb.2012.09.023

Nomenclature

c_i, c_j	concentration of a given organic compound, mol L^{-1}
c_s	bulk concentration of solids in the liquid phase, kg L^{-1}
$c_{\bullet OH}$	concentration of hydroxyl radicals, mol L^{-1}
B	peak width in XRD, nm
I_o	fluence rate at reactor wall, W m^{-2}
k_d, k_i, k	first order rate constants, s^{-1}
$k_{\bullet OH}$	second order rate constant for the reaction with hydroxyl radicals, M^{-1} s^{-1}
k_{h+}	first-order rate constant for the reaction with catalyst holes, s^{-1}
k_T	kinetic constant of the photocatalytic process, mol W^{-1} s^{-1}
K	equilibrium constant, L mol^{-1}
K_S	Scherrer constant, dimensionless
L	crystallite size, nm
LVRPA	Local Volumetric Rate of Photon Absorption, W L^{-1}
r_d	rate of direct photolysis, mol L^{-1} s^{-1}
r_i	homogeneous rate of photocatalysis, mol L^{-1} s^{-1}

Greek letters

δ	optical path, m
κ	specific absorption coefficient, m^{-2} kg^{-1}
κ_i	extinction coefficient for compound i, M^{-1} m^{-1}
λ	wavelength, Å or nm
σ	specific scattering coefficient, m^{-2} kg^{-1}
ω	scattering albedo, $\sigma/(\sigma+\kappa)$, dimensionless

Several studies have indicated that advanced oxidation processes (AOP) are a suitable choice for the removal of β-blockers from aqueous solution [10,11]. In particular, the oxidation of propranolol has been studied in the past using advanced oxidation processes like ozonation [12,13] radiolysis [14], UV/H_2O_2 [15] and electro-Fenton and photoelectro-Fenton [16]. Heterogeneous photocatalysis belongs to the category of AOP due to the formation of surface reactive oxygen species (ROS) such as the radicals $HO^{\bullet}$, $O_2^{\bullet-}$ or $HO_2^{\bullet}$. In this process, the irradiation of certain semiconductors in the presence of oxygen creates a redox environment suitable for the oxidation of diluted organic pollutants [17]. The most common photocatalyst is titanium dioxide, the performance of which is very well documented [18]. Titanium dioxide, however, only absorbs the near-UV part of the solar spectrum (wavelength shorter than 390 nm) corresponding to the band gap of TiO_2, which is about 3.2 eV depending on the anatase/rutile ratio, or even higher for nanoparticles. This fact represents a major drawback for the development of solar photocatalysis, an environmentally friendly process which could reduce the impact of energy consumption related to the use of UV lamps [19]. The photocatalytic efficiency of titanium dioxide can be enhanced by red shifting its absorption to the visible region (400–800 nm), which can be achieved by doping the anatase matrix with certain cationic or anionic impurities. Rare earth oxides, in particular, enhance the photocatalytic activity of TiO_2 due to the transitions of 4f electrons, which can increase the separation rate of photogenerated charges [20]. Cerium has also been identified as one of the most interesting rare earth dopants due to its ability to shift between Ce^{4+} (CeO_2) and Ce^{3+} (Ce_2O_3) under oxidizing or reducing conditions and to the facile formation of labile oxygen vacancies as a result of the relatively high mobility of bulk oxygen species. Electronically, the effect of cerium on the TiO_2 bandgap has been interpreted as being due to an n-type impurity band at the interface between the titanium and cerium oxides [21].

In this study, the use of cerium-doped titanium dioxide was examined as a strategy to increase the degradation rate of the β-blocker propranolol under irradiation in the visible region. The catalyst was prepared by the sol–gel method, a method that has been extensively employed to prepare doped TiO_2 catalysts. Other methods such as hydrothermal, solvothermal or impregnation have been described elsewhere [22]. The experiments were carried out in ultrapure water and in a biologically treated wastewater from the secondary effluent of a WWTP spiked with propranolol. Besides obtaining photocatalytic kinetics, a number of reaction intermediates were detected by means of exact mass measurements performed by liquid chromatography coupled to quadrupole-time-of-flight mass spectrometry (LC-ESI-QTOF–MS/MS). Their relative abundance was assessed either in catalytic and non-catalytic runs. Finally, the toxicity of partially oxidized mixtures was determined using the green algae *Pseudokirchneriella subcapitata* and the bioluminescent marine bacterium *Vibrio fischeri*.

2. Materials and methods

2.1. Materials

Propranolol (PRO) and p-chlorobenzoic acid (pCBA) were purchased from Sigma–Aldrich (+99% purity). Titanium isopropoxide, ethanol, diammonium cerium (IV) nitrate, $[(NH_4)_2Ce(NO_3)_6]$, sodium phosphate monobasic dihydrate, sodium hydrogen phosphate, sodium hydroxide and hydrochloric acid were analytical grade reagents used as received. Pure water was obtained from a Millipore Milli-Q System with a resistivity of at least 18 MΩ cm at 25 °C. Wastewater was collected from the secondary clarifier of a wastewater treatment plant (WWTP) located in Gavà-Viladecans (Barcelona), which receives a mixture of domestic and industrial wastewater from facilities located around the area. This WWTP has a capacity of 300,000 equivalent inhabitants and was designed to treat a maximum volume of wastewater of 64,000 m^3 day^{-1}. The main characteristics of the treated wastewater are shown in Table 1.

2.2. Catalyst preparation and characterization

The photocatalyst was a cerium doped titanium oxide with different percentages of cerium (0%, 0.5% and 1%) prepared by the sol–gel method. Briefly 10 mL of titanium isopropoxide was dissolved in 50 mL of absolute ethanol (Solution A). In parallel, 92 mg of $(NH_4)_2Ce(NO_3)_6$ was dissolved in 10 mL distilled water and then added to 40 mL of ethanol and 10 mL of anhydrous acetic acid (Solution B). Solution A was then added dropwise to a beaker containing Solution B. The precipitate was dried at 100 °C and calcined at 670 °C for one hour. The calcination temperature was selected as optimal in the 500–670 °C range based on the production of hydroxyl radicals as indicated below. The amounts mentioned produced approximately 2 g of 0.5% Ce–TiO_2 catalyst.

The Brunauer–Emmet–Teller (BET) surface areas were 1.4, 34.1, 56.2 m^2/g for 0%, 0.5% and 1% Ce–TiO_2 catalysts respectively. BET surface area showed a high correlation with cerium loading. This was attributed to the decreasing particle size of crystals as discussed below. All samples showed a well-defined IUPAC type IV isotherm and average pore diameters calculated using the Barrett–Joyner–Halenda (BJH) analysis of the desorption branch showed an increase in pore diameter with cerium loadings from 8.6 nm for 0.5% Ce to 12.0 nm for 1% Ce compared with 3.7 nm for non-doped TiO_2. This behavior may be explained by the decrease in crystallite size due to the incorporation of cerium, as discussed below.

The absorbance of the photocatalyst was measured using a UV/VIS/NIR PerkinElmer Lambda 900 spectrometer equipped with

Table 1
Main wastewater parameters.

pH	8.1
Turbidity (NTU)	3.2
Turbidity of 0.45 μm filtered water for experiments (NTU)	0.75
UV absorbance at 254 nm of filtered wastewater	0.23
Total suspended solids (mg/L)	8.0
Conductivity (μS/cm) at 25 °C	2750
COD (mg/L)	35
NPOC (mg/L)	12.3
Anions and cations (mg/L)	
Chloride	589
Nitrite	9.9
Nitrate	30.1
Sulfate	205
Phosphate	9.2
Sodium	172
Potassium	45
Magnesium	45
Calcium	124
Ammonium	<0.5
Alkalinity (mg/L of $CaCO_3$)	290
Metals (ng/L)	
Chromium	335
Cobalt	840
Copper	320
Manganese	623
Molybdenum	1796
Nickel	3683
Iron	1796
Palladium	161
Silver	12
Tin	88
Titanium	277
Vanadium	25
Zinc	4233
Zirconium	113
Toxicity	
Growth inhibition of *P. Subcapitata* (%)	8.4 ± 6.9
Bioluminescence inhibition of *V. fischeri* (%)	45.8 ± 4.0

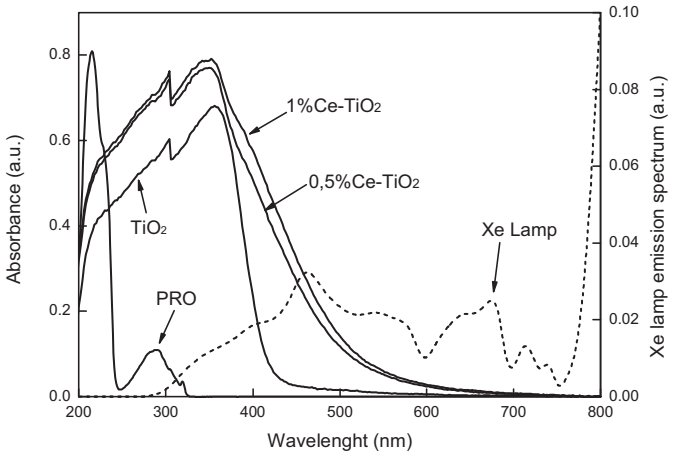

Fig. 1. Catalyst absorbance for different cerium content: (1) 1.0%, (2) 0.5%, (3) 0% (TiO_2), Xe lamp emission spectrum and propranolol absorption spectrum (5 mg/L).

an integrating sphere. The spectra are shown in Fig. 1 together with the emission spectrum of the Xenon lamp corrected with Duran tube transmission in order to display an estimate of the radiation spectrum at the inner wall of the photoreactor. The incorporation of a small amount of cerium into TiO_2 significantly increased the absorption of visible light in the 400–600 nm range, which corresponds to the maximum in the lamp emission spectrum. A further increase of cerium above 0.5% did not result in enhanced radiation absorption. The band gap energies estimated by Tauc's plot were 3.06 ± 0.15 eV, 2.67 ± 0.11 eV and 2.61 ± 0.05 eV for 0%, 0.5% and 1% cerium loadings.

The catalyst was characterized by X-ray diffraction (XRD) using a Seifert 3000P diffractometer (Cu Kα, λ = 1.5406 Å). The unit cell parameters of Ce–TiO_2 were calculated considering that TiO_2 anatase belongs to the tetragonal system, whose unit cell parameters comply with the equation $1/d_{hkl}{}^2 = (h^2 + k^2)/a^2 + l^2/c^2$. The diffraction peaks from (1 0 1) and (0 0 4) planes were used, obtaining values of $a = b = 3.78$ Å and $c = 9.49$ Å, essentially coincident with those for pure anatase. We used XRD data and the Scherrer Equation to estimate the size of crystallites in the polycrystalline samples with the Scherrer constant, K_S, rounded up to 1:

$$B(2\theta) = \frac{K_S \lambda}{L \cos\theta} \quad (1)$$

The peak width, B, was determined from the full width at half maximum. The well-defined peak of (2 0 0) plane at $2\theta = 48.1^\circ$ was used to obtain crystallite sizes. With the increase of cerium XRD peaks broadened and their relative intensity decreased. This was attributed to a reduction in the average crystallite sizes, which dropped from 38 nm (0.5 wt.% Ce) to 26 nm (1.0 wt.% Ce). The doping with cerium was shown to induce a crystal lattice expansion that could suppress the growth of anatase crystals and consequently, the average crystallite size decreased [23].

The size distribution of water suspended particles was obtained using dynamic light scattering (DLS, Malvern Zetasizer Nano ZS). Zeta potential was determined by electrophoretic light scattering in the same Nano ZS instrument. All measurements were conducted at 25 °C using 2 mM phosphate buffer (pH 7.5) as dispersing medium. It was found that the size of catalyst aggregates was not significantly affected by the presence of cerium in the structure, with sizes in the 400–600 nm range irrespective of the amount of cerium. ζ-potential, however, dropped slightly from −65 ± 10 mV (TiO_2) to −48 ± 6 mV (Ce–TiO_2) in all doped samples, which displayed similar values irrespective of cerium loading.

2.3. Analytical methods

Anions were determined using a Metrohm 861 Advance Compact IC with suppressed conductivity detector, a Metrosep A Supp 4-250 analytical column and a Metrosep A Supp 4/5 precolumn with 1.8 mM Na_2CO_3 and 1.7 mM Na HCO_3 as eluents with a flow of 1 mL/min. Cations were quantified by means of a Metrosep C4 Guard/4.0 precolumn and a Metrosep C4-150/4.0 column using 1.7 mM HNO_3 and 0.7 mM dipicolinic acid as eluent with a flow of 0.9 mL/min. Dissolved metals were determined by ICP/MS using a quadrupole mass spectrometer Agilent 7700X operating at 3 MHz in helium cell gas mode. The injection volume was 20 μL for both methods. Spectrophotometric measurements to obtain UV absorption at 254 nm were carried out in a PerkinElmer UV/VIS Lambda 20 (220–700 nm range) spectrophotometer. The determination of chemical oxygen demand (COD), total suspended solids and alkalinity was performed according to the Standard Methods for the examination of Water and Wastewater [24]. The dissolved organic carbon, DOC, determined as total content of organic carbon (TOC) and non-purgeable organic carbon (NPOC) was measured using a Shimadzu TOC-VCSH analyzer. NPOC was used for wastewater samples, which had a high content of inorganic carbon. The analyses of propranolol and pCBA were performed by HPLC using a Waters Corporation apparatus equipped with a SEA18 5 μm 15 × 0.46 Teknokroma column and a Waters 996 photodiode array detector. The mobile phase was a 60:40 mixture of water acidified with phosphoric acid at pH 3.0 and acetonitrile. UV detection was carried out at 214 nm and 237 nm for propranolol and pCBA

respectively. The flow rate was 0.7 mL/min and the injection volume was 10 μL.

A liquid chromatography-electrospray ionization-quadrupole time-of-flight–mass spectrometry (LC-ESI-QTOF–MS/MS) system in positive mode was used to identify the transformation products from propranolol. Samples collected at different irradiation times during the experiments were directly analyzed without previous pre-concentration. The analytes were separated using a HPLC system (vacuum degasser, autosampler and a binary pump Agilent Series 1200, Agilent Technologies) equipped with a reversed-phase SB-C18 analytical column of 3.0 mm × 250 mm, 5 μm particle size (Agilent Technologies). 0.1% formic acid and 5% MilliQ water in acetonitrile were used as mobile phase A and 0.1% formic acid in water (pH 3.5) as mobile phase B. The elution gradient went from 10% A (3 min) to 100% A in 22 min, to be kept thereafter at 100% A for 3 min. The flow rate was 0.5 mL/min and the injection volume 20 μL. The HPLC system was connected to a quadrupole-time-of-flight mass spectrometer (Agilent 6530 Q-TOF MS, Agilent Technologies, Santa Clara, CA). The instrument was operated in the 4 GHz High Resolution Mode. Ions were generated using an electrospray ion source with Agilent Jet Stream Technology. The operation conditions were: superheated nitrogen sheath gas temperature (400 °C) at flow rate 12 L/min; nozzle voltage, 0 V; capillary, 4000 V; nebulizer, 60 psi; drying gas, 5 L/min; gas temperature, 250 °C; skimmer voltage, 65 V; octapole RF Peak, 750 V; and fragmentor (in source CID fragmentation), 90 V. The mass axis was calibrated using the mixture provided by the manufacturer throughout the m/z 40–3200 range. A second sprayer with a reference solution was used for continuous calibration in positive ion mode using the following reference masses: 121.0509 and 922.0098 m/z (resolution: 21,700 ± 500 at 922.0098 m/z). MS/MS spectra were acquired throughout the m/z 40–950 range at a scan rate of 0.5 s/spectrum. The collision energy was optimized to obtain the highest number of fragments. The full mass spectra data recorded were processed with Agilent Mass Hunter Workstation Software (version B.03.01).

2.4. Toxicity tests

Multigenerational toxicity was evaluated using an algal growth inhibition test according to the Technical Guideline OECD TG 201[25]. To this end, we cultivated the green alga *P. subcapitata* in 96-well microplates using a total volume of 200 μL. Each well contained 100 μL of sample and 100 μL of growth medium which was prepared using the required amount of concentrated OECD medium (pH adjusted to 8.0 ± 0.1) in order to ensure the same concentration of salts in all samples and controls. The microplates were placed in an algal growth chamber under continuous fluorescent illumination (approximately 100 $\mu E\,m^{-2}\,s^{-1}$), and incubated at 22 ± 1 °C. Algal growth was assessed by chlorophyll fluorescence (excitation 444 nm–emission 680 nm) using a Fluoroskan Ascent FL plate luminometer. Algae beads and culture media were purchased from Microbiotest Inc.

Acute toxicity was assessed by measuring the decrease in the constitutive bioluminescence of the marine bacterium *V. fischeri* following the procedure described in ISO 11348-3 [26]. The measurements were performed using a Fluoroskan Ascent FL plate luminometer. The incubation period used in this study was 30 min in all cases. Tests were performed at 17.9 °C ± 0.3 °C and the decrease of light was monitored using the previously mentioned microplate luminometer. We used the commercially available Biofix Lumi test (Macherey – Nagel, Germany). The bacterial reagent is supplied freeze-dried and is reconstituted and incubated at 3 °C for 5 min before use. The analysis medium was 0.34 M NaCl (2% w/v). The toxicity was measured as the percentage of inhibition with respect to the light emitted in the absence of any toxic influence after 30 min exposure.

2.5. Experimental setup and procedure

The photocatalytic reactions were carried out in a Duran tubular photoreactor placed in a Solarbox (Co.fo.me.gra 220 V 50 Hz) and irradiated by a Xe–OP lamp (Philips 1 kW) with a photon flux of $(6.19 \pm 0.20) \times 10^{-6}$ Einstein s^{-1} (290–400 nm) determined by 2,2-nitrobenzaldehyde actinometry [27,28]. The runs were performed at 25 °C. The aqueous suspension containing 25 mg/L of propranolol, was continuously driven to the photoreactor from a feeding tank and recirculated to it, at a rate of 0.65 L/min by means of a pump (Ecoline VC-280 II, Ismatec). The reason for choosing 25 mg/L as initial concentration for propranolol was to facilitate the detection of reaction intermediates and the toxicity assessment of partially oxidized mixtures in view of the toxicity of the parent compound to the microorganisms indicated in the preceding section. All connections and pipes employed were made of Teflon and/or glass material to avoid losses by adsorption. The temperature was controlled using a Huber thermostatic bath. pH was measured with a Crison GLP 22 instrument and kept constant at 7.5 ± 0.1 by using a 2 mM phosphate buffer. The possible adsorption of phosphate was considered negligible in view of the negative charge of the catalytic surface. Dissolved oxygen concentration, with an initial value of 8.0 ± 0.5 mg O_2/L, was measured by a Crison Oxi 330i WTW Oxi Cal-SL sensor. By allowing contact with air in the recirculation chamber, an almost constant concentration of dissolved oxygen was ensured throughout the runs. The catalyst concentration varied in the 0–0.25 mg/L range. Prior to the runs, the catalyst was dispersed in 400 mL of pure water using an ultrasonic homogenizer (Bandelin Sonoplus HO2070) operating at 50 W for 10 min (70% amplitude). The catalyst dispersed in the aqueous phase was allowed to circulate through the photocatalytic system for one hour. The larger particles were removed to avoid deposition within the reaction loop. The concentration of catalyst remaining in suspension was also determined after being dried at 105 °C and weighed. The effective concentration of suspended catalyst was used as bulk concentration for calculations. Propranolol solution from a concentrate was added to the aqueous suspension of the catalyst and stirred for one more hour to reach adsorption–desorption equilibrium. Then the run started. The experiments were carried out in ultrapure water and in spiked wastewater using the secondary effluent of the WWTP described before as a matrix. Samples were withdrawn for analysis at prescribed intervals.

3. Results and discussion

3.1. Kinetics

The degradation of propranolol takes place through two parallel processes: photolysis and photocatalysis. The photolysis of propranolol, quantified in runs without catalyst, is due to the absorption of radiation of a wavelength lower than 330 nm [29]. Fig. 2 shows the extent of propranolol depletion with and without catalyst. When using 0.14 g/L of 0.5 wt.% Ce–TiO_2, propranolol completely disappeared in less than 2 h of irradiation, whereas for a similar run in the absence of catalyst, about 50% of the initial propranolol was still in solution. DOC removal also increased from 3% to 17% (after 6 h of irradiation) for runs with the same amount of catalyst with respect to non-catalytic irradiation. This difference was attributed to the photons absorbed by the photocatalyst, which generate holes (h^+) and intermediate oxygen containing oxidants such as hydroxyl radicals (·OH) which oxidized organic matter. The rate of propranolol removal can be expressed as follows, where r_d and r_i

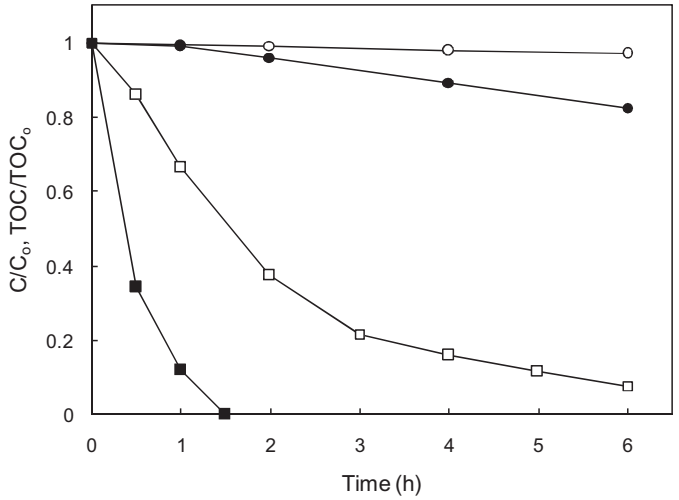

Fig. 2. Evolution of propranolol (□, ■) and TOC (○, ●) during irradiation (empty symbols) and photocatalytic oxidation (0.14 g/L, Ce–TiO_2 0.5 wt.% cerium, filled symbols).

represent the homogeneous rate of photolysis and photocatalysis respectively:

$$-\frac{dc_{PRO}}{dt} = r_d + r_i \tag{2}$$

Assuming that the heterogeneous process follows a Langmuir–Hinshelwood expression [30,31], the reaction kinetics for the rate of photocatalysis can be written as follows:

$$r_i = k_T \text{LVRPA}^m \frac{K_{PRO} c_{PRO}}{1 + \sum_i K_i c_i} \tag{3}$$

where K_{PRO} is the equilibrium constant for propranolol adsorption and k_T is a true kinetic constant independent of photon absorption that includes the primary quantum yield for electron–hole generation within the photocatalyst. The kinetic constant takes into account all other factors that may affect the overall quantum yield, with the exception of the substrate concentration and the local volumetric rate of photon absorption (LVRPA). The exponent m of the LVRPA depends on the efficiency of electron–hole formation and recombination at the catalyst surface. The data available indicate that at weak radiation intensities, the rate of photocatalytic oxidation is first-order in radiation intensity and, therefore, $m = 1$ [32]. The sum in the denominator extends to all adsorbable compounds in the mixture including unreacted propranolol. Gora et al. [33] and Li Puma et al. [34] determined that the dark equilibrium constants for the TiO_2 adsorption of several compounds were of the same order of magnitude as those observed under irradiation. They also suggested that the transformation products should have equilibrium constants similar to that of the parent compounds, all of them being essentially independent of radiation absorption. The denominator of Eq. (5) takes the following simplified form:

$$1 + \sum_i K_i c_i = 1 + \sum_i K_i c_{i,o} = 1 + K_{PRO} c_{PRO,o} \tag{4}$$

Eq. (3) is valid for any point inside the reactor. The effective radiant power absorbed within the reaction space can be obtained by integrating the LVRPA [35]:

$$\int_V \text{LVRPA}\, dV = 2\pi \int_r \int_z r(\text{LVRPA}) dr\, dz \tag{5}$$

In a reactor with recirculation with a total volume V and a reactor volume V_r, Eq. (3), yields, after integrating LVRPA, the following first-order rate expression:

$$r_i = \frac{K_{PRO}}{V} \frac{k_T \left(\int_{V_r} \text{LVRPA}\, dV_r \right)}{1 + K_{PRO} c_{PRO,o}} c_{PRO} \tag{6}$$

Finally, the LVRPA can be calculated from the two-flux-absorption-scattering model proposed by Li Puma and Brucato [35]:

$$\text{LVRPA} = \kappa c_s I_o e^{-(\kappa+\sigma) c_s \delta \sqrt{1-\omega^2}} \tag{7}$$

The presence of adsorbing compounds does not alter the scattering coefficient, σ, which is equal to that of the photocatalyst particles. In Eq. (7), κ is the specific absorption coefficient of the catalyst, ω the scattering albedo, and I_o the fluence rate at reactor wall. On the other hand, the absorption coefficient of the medium is a sum of the absorption coefficients of all dissolved compounds and the catalyst: $\kappa\, c_s + \Sigma \kappa_i\, c_i$.

The rate of the photochemical process, r_d, depends on the overall quantum yield and on the LVRPA, in which $\kappa\, c_s$ of Eq. (7) must be substituted by $\Sigma \kappa_i\, c_i$ or $\kappa_{PRO}\, c_{PRO}$.

$$r_d = \Phi_{PRO} \kappa_{PRO} c_{PRO} I_o e^{\left[-\left(\sigma c_s + \sum_i \kappa_i c_i \right) \delta \sqrt{(1-\omega^2)} \right]} \tag{8}$$

Assuming again that $\Sigma \kappa_i\, c_i$ is essentially coincident with $\kappa_{PRO}\, c_{PRO}$ due to the contribution of transformation products from the parent compound, both r_i and r_d become first-order in the concentration of propranolol, with the following global rate expression:

$$-\frac{dc_{PRO}}{dt} = (k_d + k_i) c_{PRO} = k\, c_{PRO} \tag{9}$$

It is interesting to note that, when applied to a polychromatic radiation, all relevant quantities, namely absorption and scattering coefficients and quantum yield, have to be averaged over the useful spectrum of the incident radiation [36]. Also that first-order rate constants k and k_i depend on the initial concentration of propanolol.

Photocatalytic runs were performed with a Ce–TiO_2 using different cerium loadings: 0, 0.5 and 1.0 wt.%, the effective bulk catalyst concentration varying in the 0–0.27 g/L range. Fig. 3 shows the

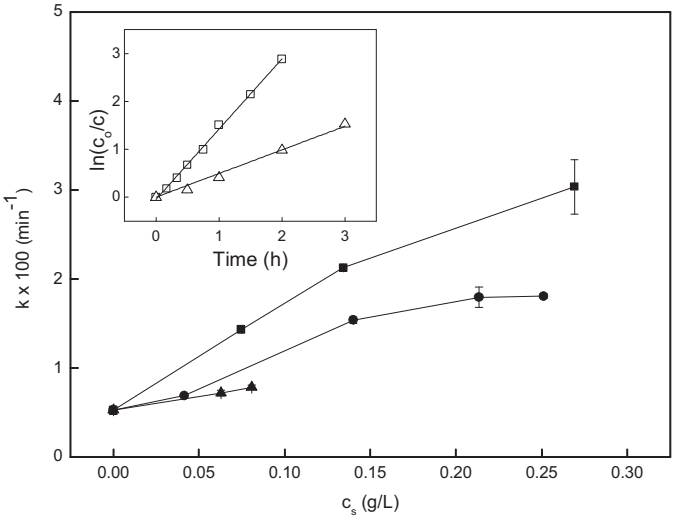

Fig. 3. First-order rate constant as a function of bulk catalyst concentration for different cerium loadings: 1.0 wt.% (●), 0.5 wt.% (■) and TiO_2 without cerium (▲). Inset: fitting of the logarithmic concentration decay for pure irradiation (without catalyst, Δ) and for 75 μg/L Ce–TiO_2, 0.5 wt.% Ce. (pH 7.5, 2 mM phosphate buffer.)

increase in the first-order rate constant of propranolol degradation using cerium-doped catalysts with respect to non-doped TiO_2. As indicated in Fig. 1, the presence of cerium shifted the absorption towards higher wavelengths, which is probably the reason of their improved performance. The best results were obtained for photocatalysts with a cerium loading of 0.5 wt.% and rate constants roughly twice those of 1.0 wt.% cerium loading. This behavior was probably due to the role played by Ce^{4+} in suppressing electron–hole recombination, which turns into a combination centre at higher dopant concentrations leading to a decrease in photocatalytic activity [23]. Li et al. [37] suggested that the presence of Ce^{4+} on catalyst surface may promote the production of hydroxyl radicals from dissolved oxygen increasing the efficiency by which a photogenerated electron is transferred. It has also been pointed out that the formation of an amorphous Ce–Ti–O phase at high cerium loadings has a detrimental effect on the dopant role in preventing electron–hole recombination [38].

On the other hand, the decrease in crystallite size results in the creation of oxygen vacancies which could reduce recombination, this being consistent with our observations concerning crystallite size in doped TiO_2 [23]. The inset in Fig. 3 shows the fitting to a first-order rate equation of catalytic and non-catalytic runs. The rate constant increased with catalyst load in all cases, as indicated in Fig. 3, in which the error bars represent 95% confidence intervals. The relationship was essentially linear, as expected from the dependency of rate constants on bulk catalyst concentration, c_s, expressed in Eq. (7).

The degree of mineralization, measured through dissolved organic carbon (DOC), was 8.5% and 17.4% for catalysts with 1.0 and 0.5 of cerium wt.% respectively after six hours of irradiation using a catalyst concentration of 0.14 g/L. The behavior was similar in other conditions, with the catalyst doped with 0.5 wt.% cerium being the most effective in all cases. Although higher catalyst concentrations (up to 0.27 g/L) led to higher rate constants, we chose the concentration of 0.14 g/L because if fell in the region in which the rate constant increased linearly with catalyst loading. It is well-known that up to a certain catalyst loading the specific reaction rate starts to decline, a fact that can be attributed to the shielding effect or obstruction of light transmission, but also to the appearance of internal mass-transfer limitations within particles [39].

The contribution of hydroxyl radicals to propranolol degradation was assessed employing a competitive kinetic approach with pCBA as hydroxyl radical probe. pCBA has been reported for this purpose in UV studies due to its rapid reaction with •OH ($k_{\bullet OH,pCBA} = 5 \times 10^9\ M^{-1}\ s^{-1}$) and its low quantum yield for direct photolysis (0.026 using wavelengths in the 250–350 nm range) and low radiation absorption above 290 nm (Duran cut-off), which implies a low rate of photolysis compared to the •OH pathway [40]. Besides, no significant adsorption of pCBA has been observed in dark contact with the photocatalyst and, therefore, the direct oxidation of pCBA by holes was considered negligible, the compound being only depleted by bulk hydroxyl radicals. Following Elovitz and von Gunten, the exposure to •OH could be obtained from kinetic data as follows [41]:

$$\ln\frac{c_{pCBA,o}}{c_{pCBA}} = k_{OH,pCBA}\int c_{\bullet OH}dt \tag{10}$$

Coming back to Eq. (9), the apparent first-order constant for photocatalysis, k_i, is the consequence of two contributions: the oxidation of compounds adsorbed in catalyst holes, $k_{i,h+}$, and the bulk reaction intermediated by hydroxyl radicals $k_{i,\bullet OH}$:

$$-\frac{dc_{PRO}}{dt} = (k_d + k_{i,h+} + k_{i,\bullet OH}c_{\bullet OH})c_{PRO} \tag{11}$$

Integrating Eq. (11), and combining it with Eq. (10), it is possible to relate the logarithmic concentration decay rates of propranolol and pCBA:

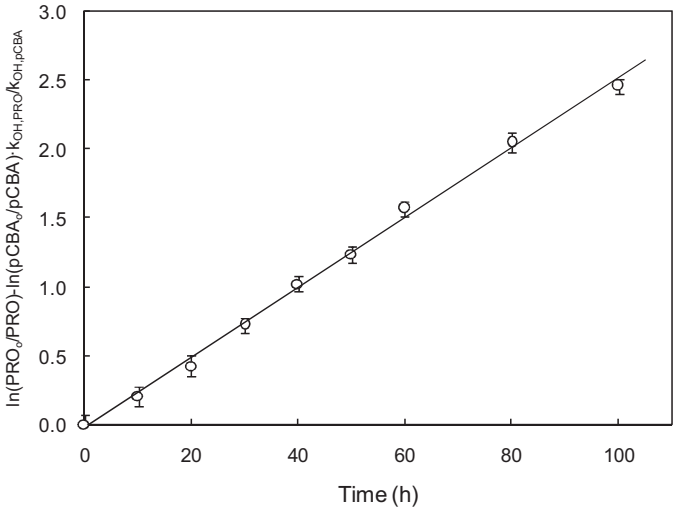

Fig. 4. Fitting of competitive kinetics (Eq. (12)) for the simultaneous treatment of propranolol and pCBA with 0.14 mg/L Ce–TiO_2, 0.5 wt.% Ce.

$$\ln\frac{c_{PRO,o}}{c_{PRO}} = (k_d + k_{i,h+})t + k_{i,\bullet OH}\int c_{\bullet OH}dt = (k_d + k_{i,h+})t + \frac{k_{i,\bullet OH}}{k_{OH,pCBA}}\ln\frac{c_{pCBA,o}}{c_{pCBA}} \tag{12}$$

The second order rate constant for the reaction of propranolol and hydroxyl radicals, $k_{i,\bullet OH}$, was measured by Benner et al. who reported a value of $1.0 \pm 0.2 \times 10^{10}\ M^{-1}\ s^{-1}$ [42]. By plotting the time-independent terms of Eq. 12 as a function of time (Fig. 4), the slope yields the experimental value of $k_d + k_{i,h+}$, the sum of the first-order rate constants for direct photolysis and photocatalytic oxidation of propranolol in catalyst holes, $k_{i,h+}$. The result was $2.50 \times 10^{-2} \pm 4 \times 10^{-4}\ min^{-1}$, and by subtracting the experimental value of k_d ($8.2 \times 10^{-3} \pm 6 \times 10^{-4}\ min^{-1}$), the calculated rate constant for the reaction with holes was $1.6 \times 10^{-2} \pm 1 \times 10^{-3}\ min^{-1}$. It was assumed that a low fraction of radiation is absorbed by the catalyst. On the other hand, the rate constant, k, for the photocatalytic degradation of propranolol under the same conditions was $3.53 \times 10^{-2} \pm 3 \times 10^{-4}\ min^{-1}$ (Fig. 3). Combining the former results, $k_i = k_{i\bullet OH}\ c_{\bullet OH} = 1.03 \times 10^{-2} \pm 7 \times 10^{-4}\ min^{-1}$ and, therefore, it can be estimated that 60% of the photocatalytic reaction took place through surface holes (h+) for a catalyst load of 0.14 g/L, the rest being mediated by hydroxyl radicals. Yang et al. calculated that 77.5% of the UV-TiO_2 degradation of propranolol was due to the reaction with hydroxyl radicals, with 19.2% being due to the reaction with oxidizing catalyst holes [30]. The difference was probably due to the different catalyst load (one order of magnitude greater) which could leave a high catalyst surface area free to produce hydroxyl radicals from water, and to the different light source (UV instead of visible light). Adsorption experiments performed in the dark enabled us to calculate that under the aforementioned conditions, about 20% of the propranolol in solution became adsorbed on the catalyst surface (pH 7.5, buffered). This high adsorption, shared by other β-blockers as noted by Yang et al. suggest that degradation is prone to occur mainly on the surface of TiO_2 by oxidation with holes [30]. These ideas are supported by the fact that experimental runs with Ce–TiO_2 resulted in a lower rate constant when performing runs at pH 6 in comparison with pH 7.5 (23% lower).

Photocatalytic degradation runs were also performed using a wastewater matrix with the Ce–TiO_2 (0.5 wt.% Ce) and a catalyst bulk concentration of 0.14 g/L. The results are shown in Fig. 5. In

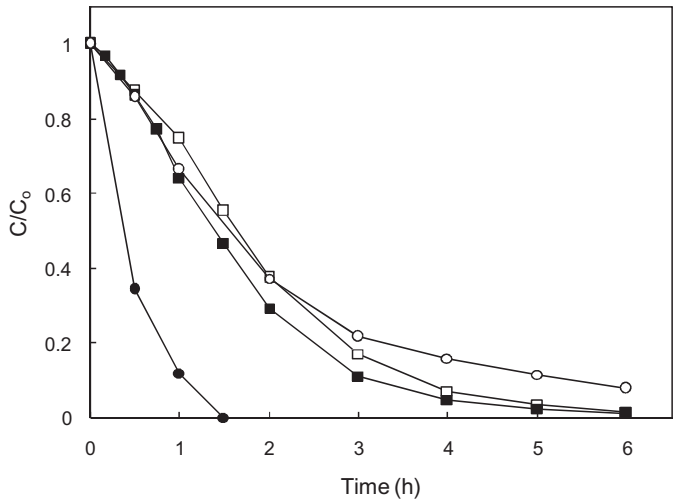

Fig. 5. Propranolol depletion for irradiation (□) and photocatalytic (■,0.14 g/L, Ce–TiO_2 0.5 wt.% Ce) runs in spiked wastewater. For comparison similar runs in pure water are included (○, ●), filled symbols representing photocatalytic experiments.

photolytic runs without catalyst, it was observed that the first-order rate constant, k_d, was higher than that of the runs performed in pure water (85% higher). This was probably due to the consequence of the photolysis of nitrate and nitrite, which has been shown to induce the formation of hydroxyl radicals by absorbing light at 360 nm and 310 nm respectively [43]. It has also been shown that the presence of organic matter in wastewater effluents may also contribute to the photochemical formation of hydroxyl radicals [44]. First-order catalytic rate constants, k, were higher than those of pure photolytic runs (15% higher), but the difference was much lower than that encountered in experiments performed in pure water, in which the catalyst increased the degradation rate by up to four times. This dramatic decrease in the efficiency of the photocatalyst, reflected in k_i values dropping from $1.71 \pm 0.15\ min^{-1}$ to $0.06 \pm 0.01\ min^{-1}$, was probably in part a consequence of the presence of radical scavengers in wastewater, such as bicarbonates, phosphates or organic matter. The important role played by catalytic holes in reactions performed in pure water suggests that other compounds in wastewater compete with propranolol for surface adsorption, which would explain this reduction in efficiency. Dimitroula et al. also found a decrease in the oxidation rate of several micropollutants of one order of magnitude when comparing the reaction in pure water with a wastewater matrix [45]. Ioannou et al. showed that mineralization practically did not take place at all when irradiating β-blockers with solar light in the presence of TiO_2 [46]. They assumed that photo-generated reactive species were consumed by attacking organic compounds without converting them into carbon dioxide and in the reaction with chlorides and other scavengers. As a consequence, the conversion of propranolol approached zero (from 20 to 30% when dissolving it in a secondary treated wastewater effluent. Similar results have been reported elsewhere. Dialynas et al. reported that the organic matter contained in treated wastewater is considerably refractory towards photocatalytic oxidation, with a very low removal rate of dissolved organic carbon [47]. Our COD results point in the same direction and showed a 13% decrease (28% in pure water), which was essentially the same value obtained without catalyst. However, concerning DOC, we obtained a 14% decrease after 6 h (0.14 g/L, 0.5 wt.% Ce–TiO_2), only somewhat lower than that in pure water (17%, Fig. 2) and considerably higher than that of pure irradiation runs (<5%).

3.2. Identification of reaction intermediates and reaction pathway

The identification of propranolol transformation products was performed on samples with 25 mg/L of propranolol. In catalytic runs, 0.14 g/L of 0.5 wt.% Ce–TiO_2 was used. The assignment was based on accurate mass measurements recorded by the LC-QTOF–MS/MS instrument described above, operating in positive mode (ESI+). MS/MS spectra were acquired at optimized collision energies to increase fragmentation and thus improve structural information. These measurements allowed elemental compositions to be proposed for the protonated $[M+H]^+$ molecular ions and their characteristic product ions, thus providing a high degree of confidence in structure assignation. Table 2 displays the ion formula and calculated mass of the product ions, as well as relative mass error and DBE (double bond and ring equivalents). The second column of the table indicates "c" and "s" for transformation products identified in photocatalytic runs and solar irradiation respectively. "p" stands for the parent compound, propranolol, for which the accurate mass measurements recorded (m/z 260.1645 for $C_{16}H_{22}NO_2$) offer an excellent agreement of less than 1 ppm error, with calculated m/z value. Propranolol product ions yielded characteristic signals at m/z 218.1176, 183.0804 and 157.0648 that corresponded to cleavages in the aliphatic chain of isopropyl, aminoisopropyl plus water, and C_2H_2 groups, respectively (Table 2). These fragments still retained the naphthalene structure. Additionally, product ions at m/z 116.1070, 98.0964, 74.0600, 72.0808 and 56.0495 correspond to transformations in the side chain after cleavage of the ether bond of propranolol. As with propranolol, the characteristic fragmentation of oxidation by-products provided enough information for the identification of over thirty transformation products. The appearance of characteristic fragments in the set of product ions spectra indicates the prevalence of a certain fraction of the molecule and suggests the place it should occupy in the transformation pathway, a proposal which is depicted in Fig. 6. Compounds P2, P3, P5 and P21 were only encountered in samples from photocatalytic runs, the rest having been detected in all samples.

The relative abundance of the main identified compounds is given in Fig. 7. The most abundant transformation product obtained in photocatalytic runs was P4 (m/z 134.1176, $C_6H_{16}NO_2$), which is attributed to the cleavage of the ether bond of propranolol. Yang et al. studied the TiO_2 photocatalytic degradation of propranolol (and other β-blockers) and found that the main degradation products corresponded to hydroxylated forms or the parent molecule [30]. They detected several monohydroxylated and polyhydroxylated isomers as well as the product of the ether cleavage. The latter resulted in the formation of naphthol and an intermediate whose protonated form was detected at m/z 134 assumed to be an aminodiol with ion formula ($C_6H_{16}NO_2$), which corresponds with P4. The addition of hydroxyl groups to the aromatic nuclei was probably the first step in the degradation pathway. The first photoproducts identified in this study were the isomers P11–P16 ($C_{16}H_{22}NO_3$, m/z 276.1594), which represent the addition of 16 mass units to the parent compound, imputable to monohydroxylated intermediates. P11–P16, however, represented only a very low amount of the whole set of transformation products detected in photocatalytic runs, none of them being among the fourteen displaying higher chromatographic areas and included in Fig. 7a and b. In contrast, P11, P13 and P14 were measured in relatively high amounts in the photoproducts of solar irradiation (Fig. 7c and d). The main products of photocatalysis retaining the structure of propranolol were P26 (m/z 294.1700, $C_{16}H_{24}NO_4$), P27 (m/z 308.1492, $C_{16}H_{22}NO_5$), and P29 (m/z 310.1649, $C_{16}H_{24}NO_5$) all of which are the consequence of the ring-opening attack of hydroxyl radicals on the naphthol moiety.

Table 2
LC-ESI-QTOF–MS/MS mass measurements of propranolol and its transformation products and structures proposed for them (p = parent compound; c = photocatalytic process; s = solar irradiation).

Compound		R_t(min)	Ion mass (m/z)	Ion formula	Error (ppm)	DBE	Proposed structure
Propranolol – P1	p	14.83	260.1645	$C_{16}H_{22}NO_2$	−0.52	7	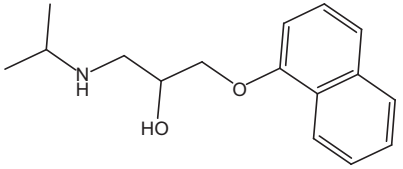
			218.1176	$C_{13}H_{16}NO_2$	1.32	6.5	
			183.0804	$C_{13}H_{11}O$	2.52	8.5	
			157.0648	$C_{11}H_9O$	−3.12	7.5	
			116.107	$C_6H_{14}NO$	−4.85	0.5	
			98.0964	$C_6H_{12}N$	1.69	1.5	
			74.06	C_3H_8NO	−3.25	0.5	
			72.0808	$C_4H_{10}N$	−2.69	0.5	
			56.0495	C_3H_6N	−4.69	1.5	
P2	c	2.26	118.0863	$C_5H_{12}NO_2$	−0.89	1	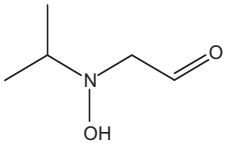
			76.0394	$C_2H_6NO_2$	1.02	0.5	
			72.0808	$C_4H_{10}N$	−3.7	0.5	
			43.0542	C_3H_7	−8.5	0.5	
P3	c	2.31	132.1019	$C_6H_{14}NO_2$	−1.44	1	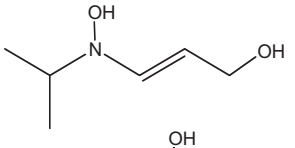
			116.107	$C_6H_{14}NO$	4.91	0.5	
			74.06	C_3H_8NO	−0.51	0.5	
			72.0808	$C_4H_{10}N$	−7.82	0.5	
			56.0495	C_3H_6N	−15.77	1.5	
P4	c—s	2.12	134.1176	$C_6H_{16}NO_2$	−0.32	0	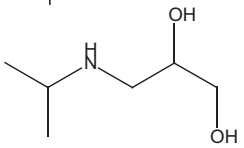
			116.107	$C_6H_{14}NO$	2.14	0.5	
			98.0964	$C_6H_{12}N$	−3.27	1.5	
			74.06	C_3H_8NO	−5.68	0.5	
			72.0808	$C_4H_{10}N$	−4.49	0.5	
			56.0495	C_3H_6N	−7.1	1.5	
P5	c	2.09	150.1125	$C_6H_{16}NO_3$	0.67	0	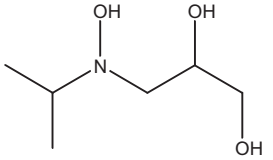
			132.1019	$C_6H_{14}NO_2$	0.92	0.5	
			114.0913	$C_6H_{12}NO$	1.5	1.5	
			88.0757	$C_4H_{10}NO$	2.56	0.5	
			74.06	C_3H_8NO	−0.9	0.5	
			72.0808	$C_4H_{10}N$	−4.01	0.5	
			56.0495	C_3H_6N	3.8	1.5	
P6	c—s	2.05	164.0917	$C_6H_{14}NO_4$	−1.09	1	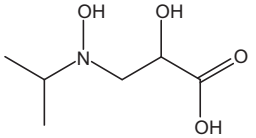
			148.0968	$C_6H_{14}NO_3$	0.05	0.5	
			146.0812	$C_6H_{12}NO_3$	1.02	1.5	
			130.0863	$C_6H_{12}NO_2$	1.87	1.5	
			128.0706	$C_6H_{10}NO_2$	−3.76	2.5	
			118.0863	$C_5H_{12}NO_2$	2.94	0.5	
			100.0757	$C_5H_{10}NO$	0.81	1.5	
			88.0757	$C_4H_{10}NO$	−2.54	0.5	
			74.0600	C_3H_8NO	−0.20	0.5	
			56.0495	C_3H_6N	−14.36	1.5	

Table 2 (*Continued*)

Compound		R_t(min)	Ion mass (m/z)	Ion formula	Error (ppm)	DBE	Proposed structure
P7	c—s	9.91	266.1387	$C_{14}H_{20}NO_4$	1.14	7	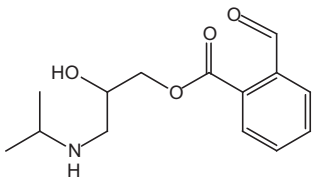
			248.1281	$C_{14}H_{18}NO_3$	2.05	6.5	
			224.0917	$C_{11}H_{14}NO_4$	4.13	5.5	
			206.0812	$C_{11}H_{12}NO_3$	1.63	6.5	
			189.0546	$C_{11}H_9O_3$	0.96	7.5	
			145.0648	$C_{10}H_9O$	−1.23	6.5	
			98.0964	$C_6H_{12}N$	−5.45	1.5	
			74.06	C_3H_8NO	4.63	0.5	
			72.0808	$C_4H_{10}N$	3.69	0.5	
			56.0495	C_3H_6N	−2.69	1.5	
P8	c—s	10.56	274.1438	$C_{16}H_{20}NO_3$	0.25	8	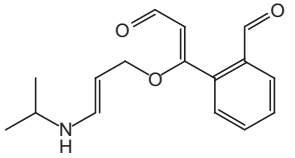
			232.0968	$C_{13}H_{14}NO_3$	2.19	7.5	
			131.0491	C_9H_7O	1.02	6.5	
			116.107	$C_6H_{14}NO$	5.59	0.5	
P9	c—s	12.13	274.1438	$C_{16}H_{20}NO_3$	−0.94	8	Structure for compounds: P9-P10
			143.0491	$C_{10}H_7O$	3.09	7.5	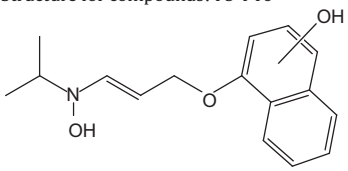
			116.107	$C_6H_{14}NO$	0.11	0.5	
			102.0913	$C_5H_{12}NO$	1.66	0.5	
			98.0964	$C_6H_{12}N$	5.2	1.5	
			72.0808	$C_4H_{10}N$	−2.93	0.5	
			56.0495	C_3H_6N	−12.49	1.5	
P10	c—s	12.47	274.1438	$C_{16}H_{20}NO_3$	−0.07	8	
			143.0491	$C_{10}H_7O$	1.47	7.5	
			116.107	$C_6H_{14}NO$	−0.87	0.5	
			102.0913	$C_5H_{12}NO$	1.66	0.5	
			98.0964	$C_6H_{12}N$	−2.43	1.5	
			72.0808	$C_4H_{10}N$	−9.2	0.5	
			56.0495	C_3H_6N	−11.21	1.5	
P11	c—s	11.08	276.1594	$C_{16}H_{22}NO_3$	1.1	7	Structure proposed for compounds: P11-P12-P13-P14-P15-P16
			258.1489	$C_{16}H_{20}NO_2$	−1.7	7.5	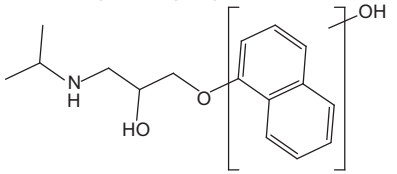
			216.1019	$C_{13}H_{14}NO_2$	3.47	7.5	
			199.0754	$C_{13}H_{11}O_2$	3.21	8.5	
			173.0597	$C_{11}H_9O_2$	−3	7.5	
			157.0648	$C_{11}H_9O$	3.17	7.5	
			116.107	$C_6H_{14}NO$	−1.2	0.5	
			102.0913	$C_5H_{12}NO$	−1.49	0.5	
			98.0964	$C_6H_{12}N$	2.34	1.5	
			72.0808	$C_4H_{10}N$	4.66	0.5	
			58.0651	C_3H_8N	−7.56	0.5	
P12	c—s	11.56	276.1594	$C_{16}H_{22}NO_3$	−2.25	7	
			258.1489	$C_{16}H_{20}NO_2$	3.2	7.5	
			216.1019	$C_{13}H_{14}NO_2$	2.63	7.5	
			199.0754	$C_{13}H_{11}O_2$	4.56	8.5	
			173.0597	$C_{11}H_9O_2$	1.26	7.5	
			157.0648	$C_{11}H_9O$	1.03	7.5	
			116.107	$C_6H_{14}NO$	2.37	0.5	
			102.0913	$C_5H_{12}NO$	1.11	0.5	
			98.0964	$C_6H_{12}N$	3.46	1.5	
			72.0808	$C_4H_{10}N$	5.62	0.5	
			58.0651	C_3H_8N	8.23	0.5	

Table 2 (*Continued*)

Compound		R_t(min)	Ion mass (m/z)	Ion formula	Error (ppm)	DBE	Proposed structure
P13	c—s	11.66	276.1594	$C_{16}H_{22}NO_3$	−1.25	7	
			258.1489	$C_{16}H_{20}NO_2$	2.23	7.5	
			216.1019	$C_{13}H_{14}NO_2$	3.02	7.5	
			199.0754	$C_{13}H_{11}O_2$	5.23	8.5	
			173.0597	$C_{11}H_9O_2$	−0.21	7.5	
			157.0648	$C_{11}H_9O$	3.21	7.5	
			116.107	$C_6H_{14}NO$	2.23	0.5	
			102.0913	$C_5H_{12}NO$	3.32	0.5	
			98.0964	$C_6H_{12}N$	1.69	1.5	
			72.0808	$C_4H_{10}N$	4.56	0.5	
			58.0651	C_3H_8N	5.26	0.5	
P14	c—s	11.93	276.1594	$C_{16}H_{22}NO_3$	0.14	7	
			258.1489	$C_{16}H_{20}NO_2$	1.66	7.5	
			216.1019	$C_{13}H_{14}NO_2$	3.21	7.5	
			173.0597	$C_{11}H_9O_2$	3.32	7.5	
			199.0754	$C_{13}H_{11}O_2$	3.56	8.5	
			157.0648	$C_{11}H_9O$	2.39	7.5	
			116.107	$C_6H_{14}NO$	3.66	0.5	
			102.0913	$C_5H_{12}NO$	2.45	0.5	
			98.0964	$C_6H_{12}N$	3.56	1.5	
			72.0808	$C_4H_{10}N$	4.99	0.5	
			58.0651	C_3H_8N	6.02	0.5	
P15	c—s	13.20	276.1594	$C_{16}H_{22}NO_3$	0.77	7	
			258.1489	$C_{16}H_{20}NO_2$	2.05	7.5	
			216.1019	$C_{13}H_{14}NO_2$	3.46	7.5	
			199.0754	$C_{13}H_{11}O_2$	4.56	8.5	
			173.0597	$C_{11}H_9O_2$	−3	7.5	
			157.0648	$C_{11}H_9O$	4.56	7.5	
			116.107	$C_6H_{14}NO$	2.32	0.5	
			102.0913	$C_5H_{12}NO$	1.66	0.5	
			98.0964	$C_6H_{12}N$	2.36	1.5	
			72.0808	$C_4H_{10}N$	5.32	0.5	
			58.0651	C_3H_8N	4.56	0.5	
P16	c—s	14.43	276.1594	$C_{16}H_{22}NO_3$	0.08	7	
			258.1489	$C_{16}H_{20}NO_2$	−5.67	7.5	
			199.0754	$C_{13}H_{11}O_2$	2.55	8.5	
			173.0597	$C_{11}H_9O_2$	0.26	7.5	
			145.0648	$C_{10}H_9O$	10.57	6.5	
			116.107	$C_6H_{14}NO$	1.69	0.5	
			98.0964	$C_6H_{12}N$	3.63	1.5	
			72.0808	$C_4H_{10}N$	3.99	0.5	
			58.0651	C_3H_8N	11.59	0.5	
P17	c—s	6.95	282.1336	$C_{14}H_{20}NO_5$	−0.85	6	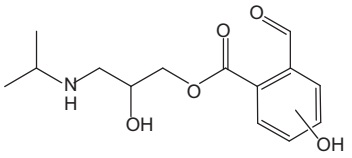
			264.123	$C_{14}H_{18}NO_4$	5.94	6.5	
			240.0866	$C_{11}H_{14}NO_5$	−1.12	5.5	
			204.0655	$C_{11}H_{10}NO_3$	−1.12	7.5	
			149.0233	$C_8H_5O_3$	3.09	6.5	
			116.107	$C_6H_{14}NO$	1.21	0.5	
			98.0964	$C_6H_{12}N$	−2.53	1.5	
			56.0495	C_3H_6N	4.32	1.5	

Table 2 (*Continued*)

Compound		R_t(min)	Ion mass (*m/z*)	Ion formula	Error (ppm)	DBE	Proposed structure
P18	c—s	7.92	282.1336	$C_{14}H_{20}NO_5$	−0.74	6	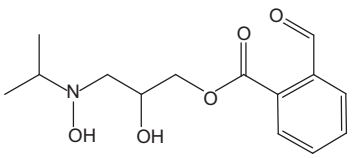
			264.123	$C_{14}H_{18}NO_4$	3.02	6.5	
			246.1125	$C_{14}H_{16}NO_3$	2.29	7.5	
			222.0761	$C_{11}H_{12}NO_4$	−0.02	6.5	
			204.0655	$C_{11}H_{10}NO_3$	7.33	7.5	
			116.107	$C_6H_{14}NO$	2.01	0.5	
			98.0964	$C_6H_{12}N$	−8.32	1.5	
			72.0808	$C_4H_{10}N$	2.1	0.5	
			56.0495	C_3H_6N	−6.41	1.5	
P19	c—s	8.77	282.1336	$C_{14}H_{20}NO_5$	−0.71	6	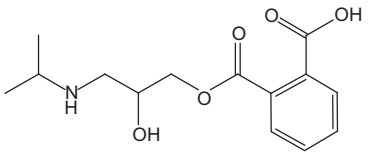
			264.123	$C_{14}H_{18}NO_4$	−6.2	6.5	
			240.0866	$C_{11}H_{14}NO_5$	1.24	5.5	
			222.0761	$C_{11}H_{12}NO_4$	−5.15	6.5	
			178.0863	$C_{10}H_{12}NO_2$	20.01	5.5	
			98.0964	$C_6H_{12}N$	5.72	1.5	
			72.0808	$C_4H_{10}N$	0.34	0.5	
			56.0495	C_3H_6N	−6.69	1.5	
P20	c—s	9.78	282.1336	$C_{14}H_{20}NO_5$	−1.89	6	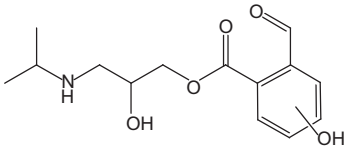
			264.123	$C_{14}H_{18}NO_4$	2.33	6.5	
			149.0233	$C_8H_5O_3$	9.04	6.5	
			116.107	$C_6H_{14}NO$	26.75	0.5	
			98.0964	$C_6H_{12}N$	−4	1.5	
			72.0808	$C_4H_{10}N$	2.1	0.5	
			56.0495	C_3H_6N	−11.68	1.5	
P21	c	8.74	292.1543	$C_{16}H_{22}NO_4$	−0.44	7	Structure proposed for compounds: P21-P22
			274.1438	$C_{16}H_{20}NO_3$	6.69	7.5	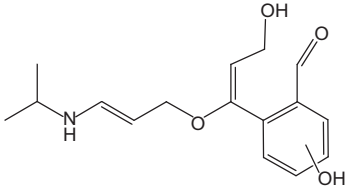
			264.1594	$C_{15}H_{22}NO_3$	4.68	5.5	
			161.0597	$C_{10}H_9O_2$	−11.89	6.5	
			116.107	$C_6H_{14}NO$	2.23	0.5	
			72.0808	$C_4H_{10}N$	4.02	0.5	
P22	c—s	8.95	292.1543	$C_{16}H_{22}NO_4$	−1.01	7	
			274.1438	$C_{16}H_{20}NO_3$	−1.86	7.5	
			264.1594	$C_{15}H_{22}NO_3$	3.95	5.5	
			187.0754	$C_{12}H_{11}O_2$	0.17	7.5	
			161.0597	$C_{10}H_9O_2$	−10.8	6.5	
			133.0648	C_9H_9O	−9.39	5.5	
			116.107	$C_6H_{14}NO$	2.23	0.5	
			98.0964	$C_6H_{12}N$	−2.35	1.5	
			72.0808	$C_4H_{10}N$	−1.23	0.5	
			56.0495	C_3H_6N	−6.39	1.5	
P23	c—s	9.69	292.1543	$C_{16}H_{22}NO_4$	−4.98	7	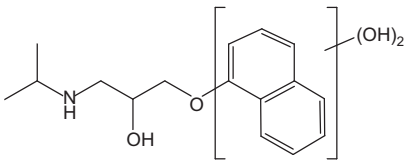
			274.1438	$C_{16}H_{20}NO_3$	1.22	7.5	
			132.1019	$C_6H_{14}NO_2$	9.47	0.5	
			116.107	$C_6H_{14}NO$	−0.56	0.5	
			98.0964	$C_6H_{12}N$	1.5	1.5	
			72.0808	$C_4H_{10}N$	−11.77	0.5	
			56.0495	C_3H_6N	−4.91	1.5	

Table 2 (*Continued*)

Compound		R_t(min)	Ion mass (m/z)	Ion formula	Error (ppm)	DBE	Proposed structure
P24	c—s	10.17	292.1543	$C_{16}H_{22}NO_4$	0.27	7	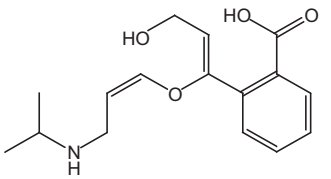
			274.1438	$C_{16}H_{20}NO_3$	−0.91	7.5	
			232.0968	$C_{13}H_{14}NO_3$	0.18	7.5	
			246.1494	$C_{15}H_{20}NO_2$	0.61	6.5	
			215.0703	$C_{13}H_{11}O_3$	8.24	8.5	
			197.0597	$C_{13}H_9O_2$	−0.22	9.5	
			185.0597	$C_{12}H_9O_2$	10.25	8.5	
			157.0648	$C_{11}H_9O$	−2.55	7.5	
			116.107	$C_6H_{14}NO$	3.21	0.5	
			72.0808	$C_4H_{10}N$	3.63	0.5	
			56.0495	C_3H_6N	−19.19	1.5	
P25	c—s	12.23	292.1543	$C_{16}H_{22}NO_4$	0.47	7	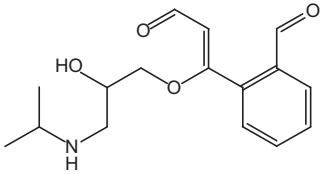
			274.1438	$C_{16}H_{20}NO_3$	0.89	7.5	
			159.0441	$C_{10}H_7O_2$	4.15	7.5	
			131.0491	C_9H_7O	−2.23	6.5	
			116.107	$C_6H_{14}NO$	3.02	0.5	
			103.0542	C_8H_7	−0.72	5.5	
			98.0964	$C_6H_{12}N$	5.22	1.5	
			72.0808	$C_4H_{10}N$	−4.01	0.5	
			56.0495	C_3H_6N	−5.92	1.5	
P26	c—s	5.07	294.1700	$C_{16}H_{24}NO_4$	−2.4	6	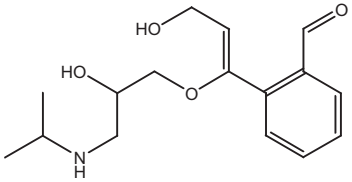
			276.1594	$C_{16}H_{22}NO_3$	1.76	6.5	
			234.1125	$C_{13}H_{16}NO_3$	−5.56	6.5	
			199.0754	$C_{13}H_{11}O_2$	−2.7	8.5	
			173.0597	$C_{11}H_9O_2$	−1.03	7.5	
			116.107	$C_6H_{14}NO$	5.32	0.5	
			98.0964	$C_6H_{12}N$	3.38	1.5	
			74.06	C_3H_8NO	−7.14	0.5	
			72.0808	$C_4H_{10}N$	2.56	0.5	
			56.0495	C_3H_6N	−12.3	1.5	
P27	c—s	11.18	308.1492	$C_{16}H_{22}NO_5$	0.53	7	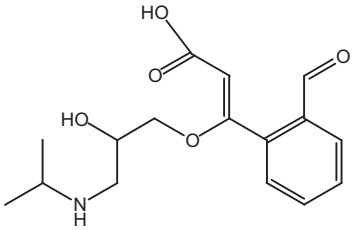
			290.1387	$C_{16}H_{20}NO_4$	4.02	7.5	
			249.0757	$C_{13}H_{13}O_5$	1.19	7.5	
			175.039	$C_{10}H_7O_3$	2.91	7.2	
			147.0446	$C_9H_7O_2$	−1.72	6.5	
			131.0491	C_9H_7O	3.72	6.5	
			116.107	$C_6H_{14}NO$	3.23	0.5	
			98.0964	$C_6H_{12}N$	2.86	1.5	
			72.0808	$C_4H_{10}N$	10.23	0.5	
			56.0495	C_3H_6N	4.02	1.5	
P28	c—s	12.02	308.1492	$C_{16}H_{22}NO_5$	0.53	7	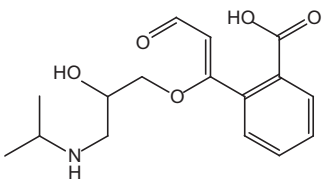
			290.1387	$C_{16}H_{20}NO_4$	−1.89	7.5	
			249.0757	$C_{13}H_{13}O_5$	−0.9	7.5	
			175.039	$C_{10}H_7O_3$	1.41	7.5	
			157.029	$C_{10}H_5O_2$	−4.07	8.5	
			131.0491	C_9H_7O	3.12	6.5	
			116.107	$C_6H_{14}NO$	1.02	0.5	
			98.0964	$C_6H_{12}N$	3.21	1.5	
			72.0808	$C_4H_{10}N$	1.23	0.5	
			56.0495	C_3H_6N	−3.76	1.5	

Table 2 (*Continued*)

Compound		R_t(min)	Ion mass (*m/z*)	Ion formula	Error (ppm)	DBE	Proposed structure
P29	c—s	3.37	310.1649	$C_{16}H_{24}NO_5$	1.36	6	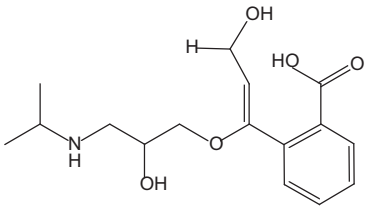
			292.1543	$C_{16}H_{22}NO_4$	1.23	7	
			274.1438	$C_{16}H_{20}NO_3$	−3.02	7.5	
			256.1338	$C_{16}H_{18}NO_2$	6.15	8.5	
			250.1079	$C_{13}H_{16}NO_4$	6.23	6.5	
			232.0974	$C_{13}H_{14}NO_3$	0.43	7.5	
			228.1388	$C_{15}H_{18}NO$	5.44	7.5	
			215.0708	$C_{13}H_{11}O_3$	−1.39	8.5	
			199.0759	$C_{13}H_{11}O_2$	−5.85	8.5	
			197.0603	$C_{13}H_9O_2$	−3.7	9.6	
			116.107	$C_6H_{14}NO$	1.23	0.5	
			114.0913	$C_{13}H_{12}NO$	4.01	1.5	
			98.0964	$C_6H_{12}N$	4.24	1.5	
			72.0808	$C_4H_{10}N$	−17.23	0.5	
P30	c—s	4.44	310.1649	$C_{16}H_{24}NO_5$	−1.09	6	Structure proposed for compounds: P30-P32
			292.1543	$C_{16}H_{22}NO_4$	0.99	7	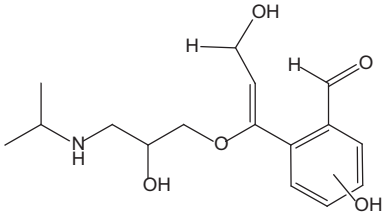
			250.1074	$C_{13}H_{16}NO_4$	−1.25	6.5	
			215.0803	$C_{13}H_{11}O_3$	2.33	8.5	
			116.107	$C_6H_{14}NO$	1.65	0.5	
			72.0808	$C_4H_{10}N$	4.63	0.5	
			56.0495	C_3H_6N	−9.32	1.5	
P31	c—s	5.97	310.1649	$C_{16}H_{24}NO_5$	1.79	6	
			292.1543	$C_{16}H_{22}NO_4$	0.36	7	
			274.1438	$C_{16}H_{20}NO_3$	1.98	7.5	
			264.1600	$C_{15}H_{22}NO_3$	5.09	5.5	
			215.0803	$C_{13}H_{11}O_3$	4.57	8.5	
			177.0552	$C_{10}H_9O_3$	−0.66	6.5	
			161.0603	$C_{10}H_9O_2$	−2.85	6.5	
			133.0653	C_9H_9O	12.43	5.5	
			116.107	$C_6H_{14}NO$	−0.14	0.5	
			98.0964	$C_6H_{12}N$	9.53	1.5	
			72.0808	$C_4H_{10}N$	−7.18	0.5	
			56.0495	C_3H_6N	−14.39	1.5	
P32	c—s	6.49	310.1649	$C_{16}H_{24}NO_5$	1.07	6	
			292.1543	$C_{16}H_{22}NO_4$	0.56	7	
			274.1438	$C_{16}H_{20}NO_3$	5.05	7.5	
			264.1600	$C_{15}H_{22}NO_3$	5.49	5.5	
			250.1079	$C_{13}H_{16}NO_4$	9.11	6.5	
			215.0803	$C_{13}H_{11}O_3$	−2.77	8.5	
			177.0552	$C_{10}H_9O_3$	−0.02	6.5	
			161.0603	$C_{10}H_9O_2$	6.1	6.5	
			133.0653	C_9H_9O	1.7	5.5	
			116.107	$C_6H_{14}NO$	−1.37	0.5	
			98.0964	$C_6H_{12}N$	−10.7	1.5	
			72.0808	$C_4H_{10}N$	2.93	0.5	
			56.0495	C_3H_6N	−3.48	1.5	

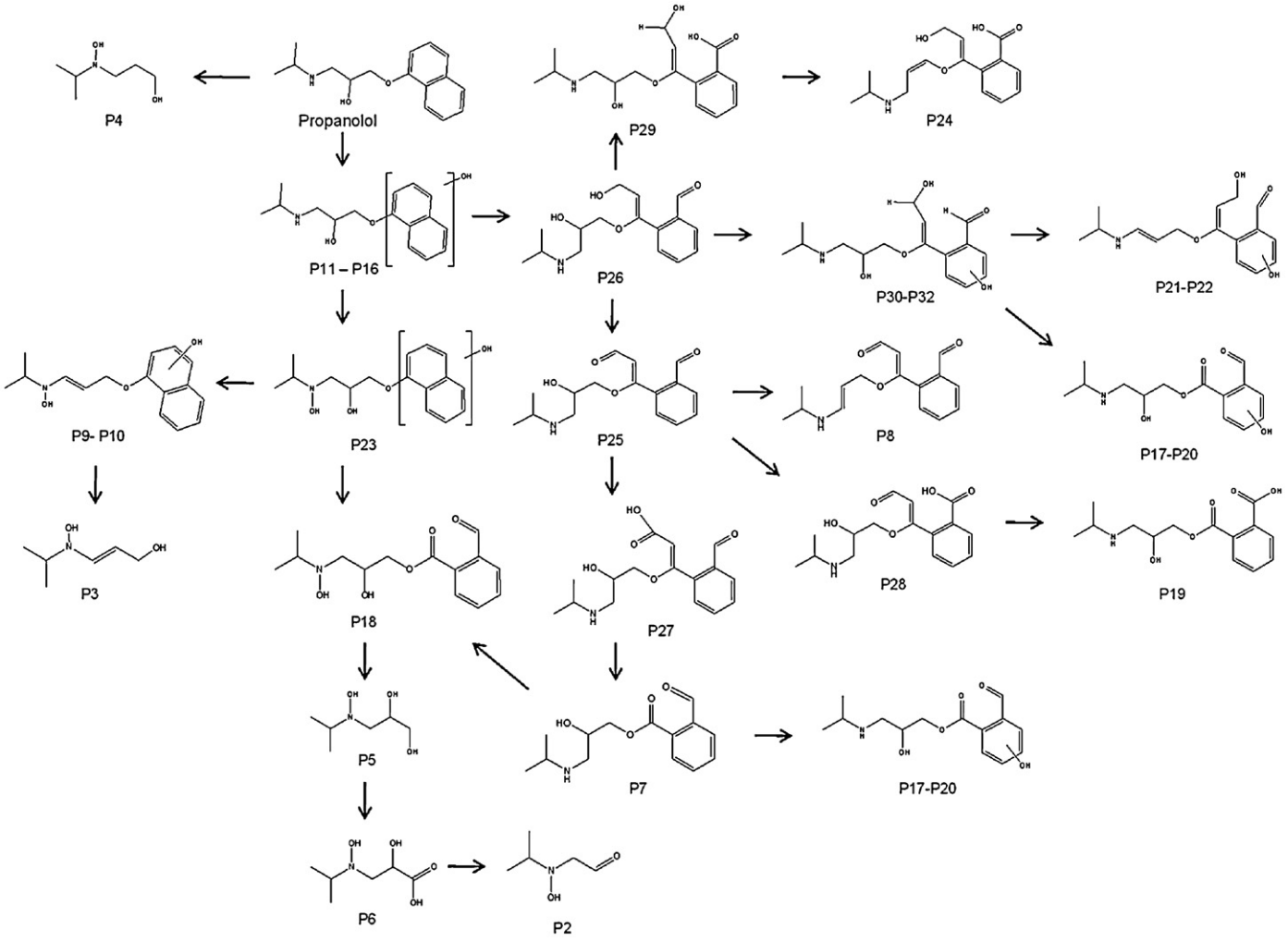

Fig. 6. Proposed degradation pathway for propranolol.

Some other fragments from the ether bond cleavage were detected in photocatalytic runs, namely P2 (*m*/*z* 118.0863, $C_5H_{12}NO_2$), P3 (*m*/*z* 132.1019, $C_6H_{14}NO_2$), P5 (*m*/*z* 150.1125, $C_6H_{16}NO_3$) and P6 (*m*/*z* 164.0917, $C_6H_{14}NO_4$), some of which were absent in non-catalytic runs. Non-catalytic solar irradiation yielded a considerably higher amount of the more complex transformation products. These included, the hydroxylated transformation products P9 and P10 (*m*/*z* 274.1438, $C_{16}H_{20}NO_3$), with a hydroxyl group in the aromatic moiety but in which the amine had been oxidized to a hydroxylamine. P25 (*m*/*z* 292.1543, $C_{16}H_{22}NO_4$) is a naphthol ring-opening product which was detected in much higher amounts in solar runs than in photocatalytic oxidation. In general, solar irradiation led to a higher accumulation of hydroxylated and polyhydroxylated intermediates (such as P23, *m*/*z* 292.1543, $C_{16}H_{22}NO_4$) in spite of a lower formation of ether cleavage products. This might be attributed to the higher oxidizing power of the photocatalytic system, which prevents the accumulation of the first oxidation intermediates. Moreover, compounds such as P4, P9 and P28, among others, tended to accumulate in the solar irradiated mixture, while exhibiting a maximum in photocatalytic runs followed by a decrease after a period of 1–3 h on stream. This is a consequence of the enhanced oxidation capacity of the photocatalytic system in comparison with pure solar irradiation.

Liu and William [48] and Liu et al. [49] studied the photodegradation of propranolol by radiation in the 295–800 nm range and determined that the main transformation product was an isomer of *m*/*z* 292 (protonated), for which they proposed a ring-opening structure. In this study, we also found a series of ring-opening products, namely P21, P22, P24 or P25 as well as a hydroxylation derivative, P23, all of them with *m*/*z* 292.1543, P25 being similar to Liu's proposal except for a different ring-opening position. Romero et al. studied the TiO_2 photocatalytic degradation of propranolol using visible light radiation [50]. They identified four reaction intermediates, of which *m*/*z* 266, 282 and 292 corresponded to our compounds P7, P18 and P25. For the others, at *m*/*z* 308, we proposed a different structure (P27–P28, $C_{16}H_{22}NO_5$) with a carboxylic acid instead of a hydroxylamine. This is justified by the presence of the characteristic fragments $C_6H_{12}N$ and $C_{10}H_7O_3$ that could not be explained otherwise. It is interesting to note that similar compounds can be obtained as a consequence of biological degradation. Marco-Urrea et al. studied the biological advanced oxidation of propranolol using the extracellular oxidizing species produced by the fungus *Trametes versicolor* [51]. The main degradation products were identified as monohydroxylated derivatives from the hydroxyl radical attack on the naphthalene moiety and would correspond to our P11–P16 set.

3.3. Toxicity of partially oxidized mixtures

Fig. 8 shows the growth inhibition of *P. subcapitata* when exposed to propranolol and partially irradiated mixtures. Growth was completely inhibited both in pure water and spiked

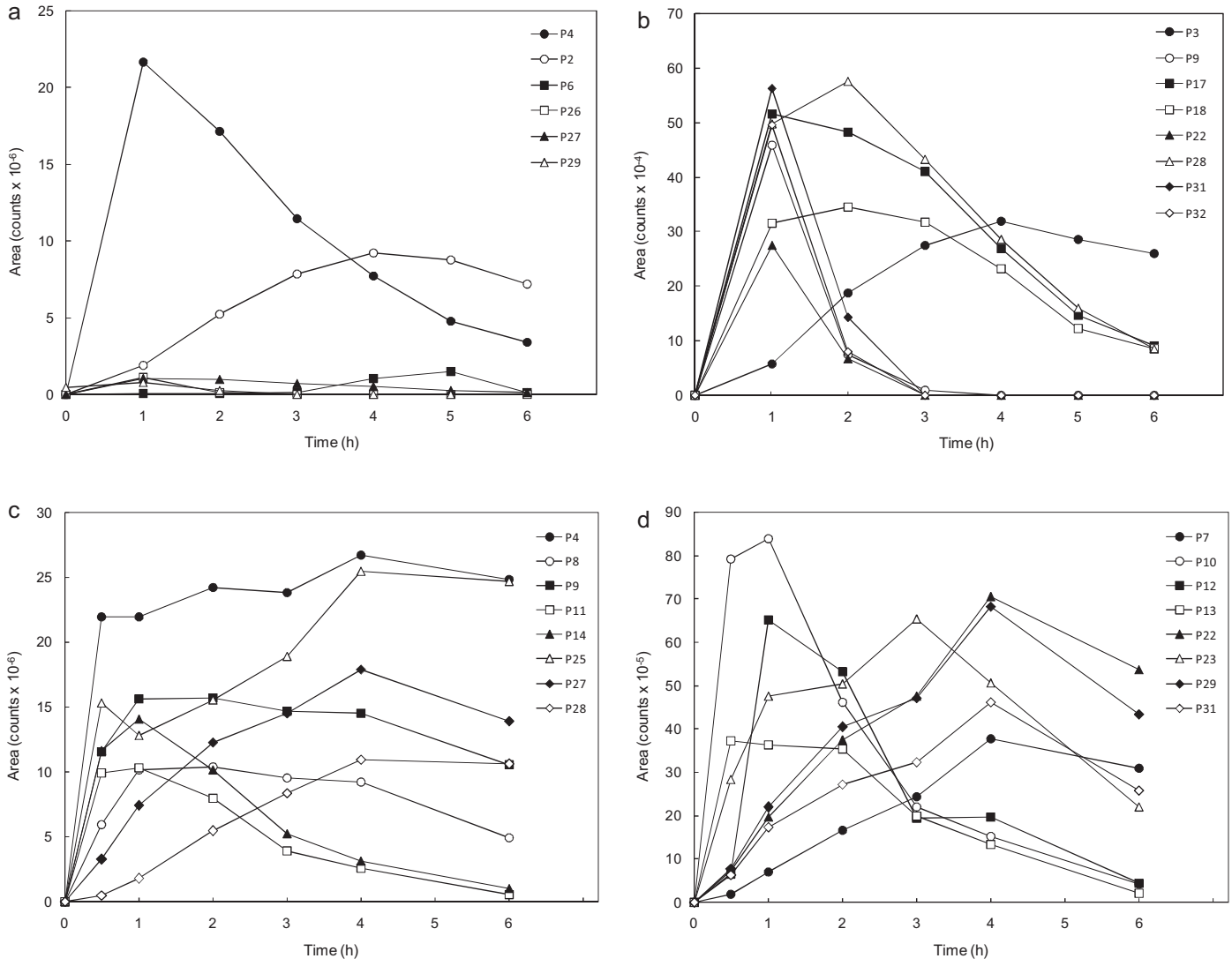

Fig. 7. Chromatographic areas of the main transformation product from photocatalytic (a, b) and solar irradiation runs (c, d).

wastewater for untreated propranolol solutions, as their concentration was considerably higher than the EC_{50} value, which is 0.77 mg/L [49]. The irradiation of propranolol decreased the toxicity towards the growth of *P. subcapitata* leading to essentially non-toxic mixtures after 2 h in the presence of 0.14 g/L of Ce–TiO_2 (0.5 Ce wt.%). For non-catalytic irradiation, the detoxification led to growth inhibition of <5% after 4 h (Fig. 8a). The effect of the presence of the catalyst was much more marked when using spiked wastewater as matrix. In this case, irradiation led to growth inhibition of still 16% after 6 h, whereas the photocatalytic process removed most of the toxicity within the first two hours (Fig. 8b). In Fig. 8b, we also represented the toxicity of irradiated wastewater that inhibited algal growth by 8%, which increased up to some 25% for prolonged exposures. It is interesting to note that during the first hour of treatment of propranolol spiked wastewater, there was no noticeable effect on mixture toxicity, which is due to the lower rate of oxidation or photodegradation in the presence of the compounds dissolved in wastewater.

Fig. 9 shows the results obtained for the marine bacteria *V. fischeri*. Escher et al. determined a median effect value of 81 mg/L for 30 min contact time of propranolol with *V. fischeri* [52]. Propranolol toxicity is much lower than for the green alga and represented a 15% inhibition for the untreated solution in pure water. The toxic effect of propranolol also increased the background toxicity of wastewater, but only to a modest 10% till about 55% bioluminescence inhibition. The non-catalytic irradiation of propranolol, either in pure water or in wastewater, resulted in a moderate toxicity reduction. The photocatalytic degradation of propranolol in pure water, however, led to a sharp bioluminescence decrease, which reached almost 80%. The fact that a similar treatment in wastewater matrix did not cause a similar toxicity peak was probably due to the accumulation of transformation products such as P17 or P28. The results with *P. subcapitata* (Fig. 8a) also show that photocatalytic treatments induce a significant increase in toxicity after about 3 h of treatment. The higher toxicity of partially oxidized mixtures was probably the consequence of the formation of ring-opening products, as these are the kinds of compound that have been associated in the past with increased toxicity in partially oxidized mixtures [53,54].

Liu et al. used the alga *P. subcapitata* and the rotifer *Brachionus calyciflorus* to conclude that propranolol yields phototransformation products that would generally be less toxic because of their higher polarity and hydrophilicity compared to the parent compound [49]. On the other hand, the formation of toxic or non-degradable compounds during the early stages of propranolol irradiation or photocatalytic oxidation has been suggested

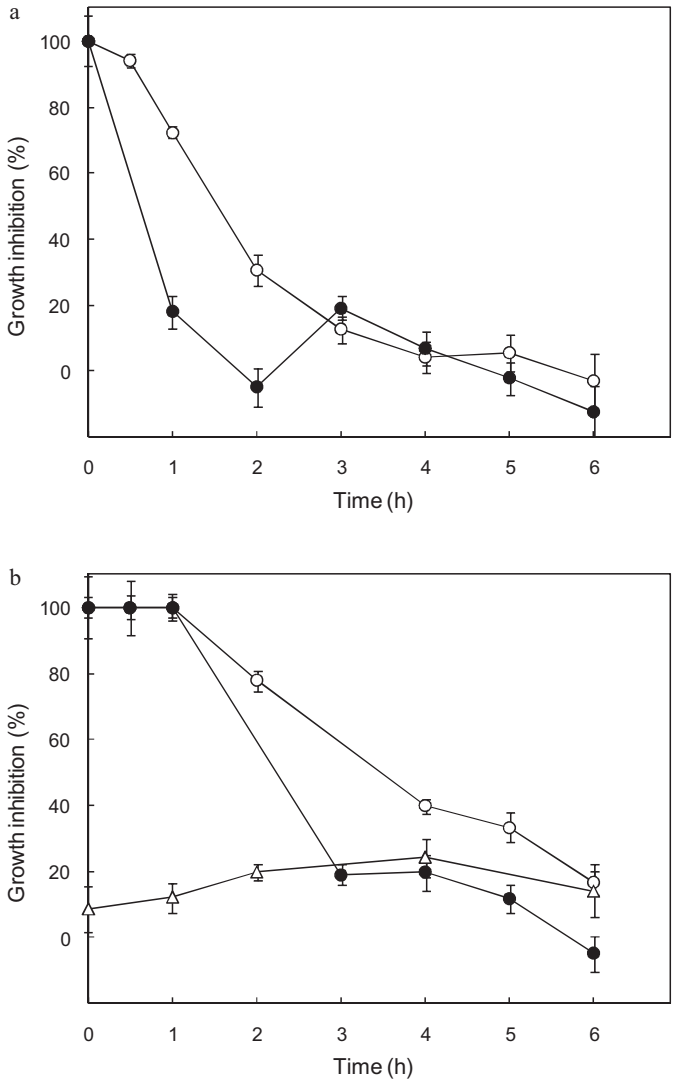

Fig. 8. Growth inhibition of *P. subcapitata* during irradiation (○) and photocatalytic treatment of propranolol (●, 0.14 g/L, Ce–TiO_2 0.5 wt.% cerium) in (a) pure water and (b) spiked wastewater. (△): toxicity of non-spiked wastewater during irradiation.

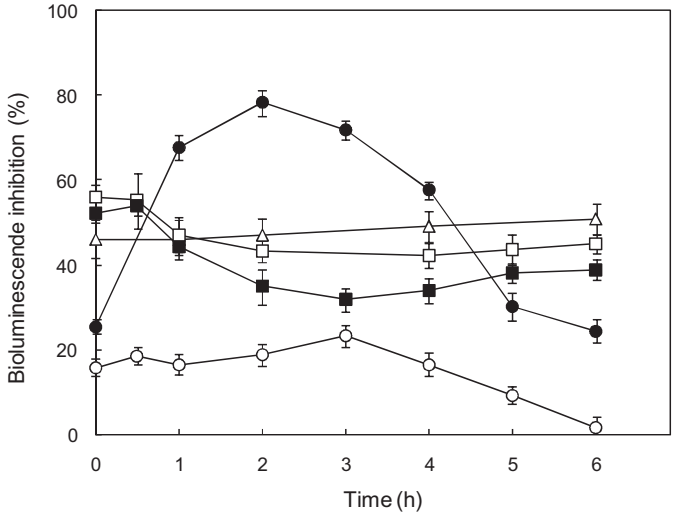

Fig. 9. Bioluminescence inhibition of *V. fischeri* during irradiation (○, □) and photocatalytic treatment of propranolol (●, ■, 0.14 g/L, Ce–TiO_2 0.5 wt.% cerium) in pure water (circles) and spiked wastewater (squares). (△): toxicity of non-spiked wastewater during irradiation.

elsewhere. Romero et al. showed that the biodegradability of visible light irradiated samples increased with time, but only after a period of several hours [50]. During the photocatalytic treatment of propranolol using TiO_2. Ioannou et al. found that the toxicity of treated mixtures to *Daphnia magna* increased during the first part of the reaction to progressively decrease thereafter [46]. This implies the formation of toxic transformation compounds that could be eliminated upon prolonged irradiation.

4. Conclusions

The visible light photocatalytic degradation of propranolol can be carried out using cerium doped titanium dioxide. The results showed that, for a cerium loading of 0.5 wt.% with a bulk catalyst concentration of 0.14 g/L, propranolol became essentially depleted after 1.5 h of irradiation. In contrast, 8% of initial propranolol remained in solution after 6 h of photolytic (non-catalytic) treatment. The effect was related to an increased light absorption in the visible region of cerium doped TiO_2.

The contribution of hydroxyl radicals to propranolol degradation was assessed using pCBA as hydroxyl radical probe. A kinetic competition approach allowed determination of the rate constant for the photocatalytic oxidation of propranolol in catalyst holes. Thus, it was estimated that 60% of the photocatalytic reaction took place through surface holes (h+), the rest being mediated by hydroxyl radicals.

Experiments carried out in biologically treated wastewater spiked with propranolol showed a very low rate for the photocatalytic process compared with pure water. This could be attributed to the presence of radical scavengers but also to substances competing for surface adsorption.

Over thirty reaction intermediates were detected by means of exact mass measurements performed by LC-ESI-QTOF–MS/MS. The main transformation products could be attributed to the cleavage of the ether bond of propranolol, while other compounds derived from the addition of hydroxyl groups to the aromatic nuclei or to the ring-opening attack of hydroxyl radicals on the naphthol moiety.

The toxicity of oxidized mixtures determined using the green algae *P. subcapitata* and bioluminescent marine bacterium *V. fischeri* showed the formation of toxic transformation products, which accumulated in runs performed in pure water, for which the photocatalytic reaction rate was much higher.

Acknowledgements

This work has been financed by Spain's Ministry of Education (CSD2006-00044) and the Dirección General de Universidades e Investigación de la Comunidad de Madrid, Research network S2009/AMB-1588. One of the authors, J.S., thanks the Spanish Ministry of Education for an FPU grant. The authors wish to thank Mar Fernández for her support with the analyses.

References

[1] K. Kümmerer, in: K. Kümmerer (Ed.), Pharmaceuticals in the Environment: Sources, Fate, Effects and Risk, Springer, New York, 2004, pp. 3–11.
[2] D.S. Maycock, C.D. Watts, in: J.O. Nriagu (Ed.), Encyclopedia of Environmental Health, Elsevier, Burlington, 2011, pp. 472–484.
[3] M. Crane, C. Watts, T. Boucard, Science of the Total Environment 367 (2006) 23–41.
[4] I. Muñoz, A. Rodríguez, R. Rosal, A.R. Fernández-Alba, Science of the Total Environment 407 (2009) 1245–1256.
[5] T.A. Ternes, Water Research 32 (1998) 3245–3260.
[6] D.B. Huggett, I.A. Khan, C.M. Foran, D. Schlenk, Environmental Pollution 121 (2003) 199–205.
[7] V. Gabet-Giraud, C. Miège, J.M. Choubert, S.M. Ruel, M. Coquery, Science of the Total Environment 408 (2010) 4257–4269.
[8] M. Maurer, B.I. Escher, P. Richle, C. Schaffner, A.C. Alder, Water Research 41 (2007) 1614–1622.

[9] R. Rosal, A. Rodríguez, J.A. Perdigón-Melón, A. Petre, E. García-Calvo, M.J. Gómez, A. Agüera, A.R. Fernández-Alba, Water Research 44 (2010) 578–588.
[10] W.H. Song, W.J. Cooper, S.P. Mezyk, J. Greaves, B.M. Peake, Environmental Science and Technology 42 (2008) 1256–1261.
[11] E. Isarain-Chávez, R.M. Rodríguez, J.A. Garrido, C. Arias, F. Centellas, P.L. Cabot, E. Brillas, Electrochimica Acta 56 (2010) 215–221.
[12] J. Benner, E. Salhi, T. Ternes, U. Gunten, Water Research 42 (2008) 3003–3012.
[13] R. Rosal, A. Rodríguez, J.A. Perdigón-Melón, M. Mezcua, M.D. Hernando, P. Letón, E. García-Calvo, A. Agüera, A.R. Fernández-Alba, Water Research 42 (2008) 3719–3728.
[14] W. Song, W.J. Cooper, S.P. Mezyk, J. Greaves, B.M. Peake, Environmental Science and Technology 42 (2008) 1256–1261.
[15] I. Kim, N. Yamashita, H. Tanaka, Chemosphere 77 (2009) 518–525.
[16] E. Isarain-Chávez, P. Lluís Cabot, F. Centellas, R.M. Rodríguez, C. Arias, J.A. Garrido, E. Brillas, Journal of Hazardous Materials 185 (2011) 1228–1235.
[17] T.E. Doll, F.H. Frimmel, Catalysis Today 101 (2005) 195–202.
[18] S. Malato, J. Blanco, A. Vidal, C. Richter, Applied Catalysis B: Environmental 37 (2002) 1–15.
[19] I. Muñoz, J. Rieradevall, F. Torrades, J. Peral, X. Domènech, Solar Energy 79 (2005) 369–375.
[20] V. Stengl, S. Bakardjieva, N. Murafa, Materials Chemistry and Physics 114 (2009) 217–226.
[21] F.B. Li, X.Z. Li, M.F. Hou, K.W. Cheah, W.C.H. Choy, Applied Catalysis A-General 285 (2005) 181–189.
[22] U.G. Akpan, B.H. Hameed, Applied Catalysis A-General 375 (2010) 1–11.
[23] S. Li, T. Chen, Z. Zhou, J. Fu, Q. Wang, Y. Wang, Nanoscale Research Letters 19 (2012) 227.
[24] American Public Health Association (APHA), American Water Works Association (AWWA) & Water Environment Federation (WEF), Standard Methods for the Examination of Water and Wastewater, 21st Edition, Washington, D.C., 2005.
[25] OECD, Test No. 201: Freshwater Alga and Cyanobacteria, Growth Inhibition Test, OECD Guidelines for the Testing of Chemicals, Section 2, OECD Publishing, 2011.
[26] International Organization for Standardization. Water Quality-Determination of the Inhibitory Effect of Water Samples on the Light Emission of *Vibrio fischeri* (Luminescent Bacteria Test). ISO 11348-3 revised version, Geneva, Switzerland, 2007.
[27] J.M. Allen, S.K. Allen, S.W. Baertschi, Journal of Pharmaceutical and Biomedical Analysis 24 (2000) 167–178.
[28] E.S. Galbavy, K. Ram, C. Anastasio, Journal of Photochemistry and Photobiology A: Chemistry 209 (2010) 186–192.
[29] R.F. Dantas, O. Rossiter, A.K.R. Teixeira, A.S.M. Simões, V.L. da Silva, Chemical Engineering Journal 158 (2010) 143–147.
[30] H. Yang, T. An, G. Li, W. Song, W.C. Cooper, H. Luo, X. Guo, Journal of Hazardous Materials 179 (2010) 834–839.
[31] C. Postigo, C. Sirtori, I. Oller, S. Malato, M.I. Maldonado, M. López, D. Barceló, Water Research 45 (2011) 4815–4826.
[32] D.F. Ollis, in: E. Pelizzetti, M. Schiavello (Eds.), Photochemical Conversion and Storage of Solar Energy, Kluver Academic Publishers, Dordrecht, 1991, pp. 593–622.
[33] A. Gora, B. Toepfer, V. Puddu, G. Li Puma, Applied Catalysis B: Environmental 65 (2006) 1–10.
[34] G. Li Puma, B. Toepfer, A. Gora, Catalysis Today 124 (2007) 124–132.
[35] G. Li Puma, A. Brucato, Catalysis Today 122 (2007) 78–90.
[36] A. Braun, M.T. Maurette, E. Oliveros, Technologie Photochimique, 1st ed., Presses Polytechiques Romandes, Lausanne, 1986.
[37] F.B. Li, X.Z. Li, M.F. Hou, W.C.H. Choi, Applied Catalysis A 285 (2005) 181–189.
[38] A.M.T. Silva, C.G. Silva, G. Drazic, J.L. Faria, Catalysis Today 144 (2009) 13–18.
[39] K. Mehrotra, G.S. Yablonsky, A.K. Ray, Industrial and Engineering Chemistry 42 (2003) 2273–2281.
[40] E.J. Rosenfeldt, K.G. Linden, S. Canonica, U. von Gunten, Water Research 40 (2006) 3695–3704.
[41] M.S. Elovitz, U. von Gunten, Ozone Science and Engineering 21 (1999) 239–260.
[42] J. Benner, E. Salhi, T. Ternes, U. von Gunten, Water Research 42 (2008) 3003–3012.
[43] J. Mack, J.R. Bolton, Journal of Photochemistry and Photobiology A: Chemistry 128 (1999) 1–13.
[44] M.M. Dong, F.L. Rosario-Ortiz, Environmental Science and Technology 46 (2012) 3788–3794.
[45] H. Dimitroula, V.M. Daskalaki, Z. Frontistis, D.I. Kondarides, P. Panagiotopoulou, N.P. Xekoukoulotakis, D. Mantzavinos, Applied Catalysis B: Environmental 117–118 (2012) 283–291.
[46] L.A. Ioannou, E. Hapeshi, M.I. Vasquez, D. Mantzavinos, D. Fatta-Kassinos, Solar Energy 85 (2011) 1915–1926.
[47] E. Dialynas, D. Mantzavinos, E. Diamadopoulos, Water Research 42 (2008) 4603–4608.
[48] Q.T. Liu, H.E. William, Environmental Science and Technology 41 (2007) 803–810.
[49] Q.T. Liu, T.D. William, R.I. Cumming, G. Holm, M.J. Hetheridge, R. Murray-Smith, Environmental Toxicology and Chemistry 28 (2009) 2622–2631.
[50] V. Romero, N. de la Cruz, R.F. Dantas, P. Marco, J. Giménez, S. Esplugas, Catalysis Today 161 (2011) 115–120.
[51] E. Marco-Urrea, J. Radjenovic, G. Caminal, M. Petrovic, T. Vicent, D. Barcelo, Water Research 44 (2010) 521–532.
[52] B.I. Escher, N. Bramaz, M. Richter, J. Lienert, Environmental Science and Technology 40 (2006) 7402–7408.
[53] R. Rosal, M.S. Gonzalo, K. Boltes, P. Letón, J.J. Vaquero, E. García-Calvo, Journal of Hazardous Materials 172 (2009) 1061–1068.
[54] J. Santiago, A. Agüera, M.M. Gómez-Ramos, A.R. Fernández Alba, E. García-Calvo, R. Rosal, Journal of Hazardous Materials 194 (2011) 30–41.